

# Supergravity and Superstring Signatures of the One-Parameter Model at LHC

James A. Maxin,<sup>1</sup> Van E. Mayes,<sup>1</sup> and Dimitri V. Nanopoulos<sup>1,2</sup>

<sup>1</sup>*George P. and Cynthia W. Mitchell Institute for Fundamental Physics, Texas A&M University,  
College Station, TX 77843, USA*

<sup>2</sup>*Astroparticle Physics Group, Houston Advanced Research Center (HARC),  
Mitchell Campus, Woodlands, TX 77381, USA;  
Academy of Athens, Division of Natural Sciences,  
28 Panepistimiou Avenue, Athens 10679, Greece*

## ABSTRACT

We investigate the allowed supersymmetry parameter space for the one-parameter model (OPM) and compute the collider signatures which may be observable at the Large Hadron Collider (LHC), taking into account the most recent experimental constraints. We find that in the strict moduli scenario, there are no regions of the parameter space which may satisfy all constraints. However, for the dilaton scenario, there are small regions of the parameter space where all constraints may be satisfied and for which the observed dark matter density may be generated. The model is thus highly predictive and/or falsifiable due to its highly constrained nature. Additionally, we compare the collider signatures of OPM to those of an intersecting  $D6$ -brane model in Type IIA string theory where the soft terms are non-universal. We find that it may be possible to discriminate between diverse types of string vacua at LHC.

## I. INTRODUCTION

With the dawn of the Large Hadron Collider (LHC) era, the prospects for the discovery of new physics may finally be arriving. In particular, whatever physics is responsible for stabilizing the electroweak scale should be discovered. Signals of the favored mechanism, broken supersymmetry, may be observed as well as the Higgs states required to break the electroweak symmetry. However, at present there is no theory which may uniquely predict the masses of the superpartners should they be observed at LHC

In principle, it should be possible to derive all known physics in a top-down approach directly from a more fundamental theory such as string theory, as well as potentially predicting new and unexpected phenomena. Conversely, following a bottom-up approach, one may ask if it is possible to deduce the origin of new physics given such a signal at LHC. For example, in the case of low-energy supersymmetry, it may be possible from the experimental data to deduce the structure of the fundamental theory at high energy scales which determines the soft-supersymmetry breaking terms and ultimately leads to radiative electroweak symmetry breaking (REWSB) [1, 2, 3].

No-scale supergravity (nSUGRA) [4] is such a framework where it is possible to naturally explain REWSB and correlate it with the gravitino mass, or more generally, the effective SUSY breaking scale. In the simplest no-scale models, the gravitino mass  $m_{3/2}$  remains undetermined at the classical level, and is instead fixed by radiative corrections to be near the electroweak scale [4]. Thus, in this framework, we find that the scale of supersymmetry breaking is correlated with the electroweak scale [4]. Another striking feature of nSUGRA is that the cosmological constant vanishes at tree-level. Although it is presently known that the cosmological constant is in fact non-zero, its very small value is still consistent with the no-scale framework with small corrections. Furthermore, it is well-known that the Kähler moduli of Type I, IIB orientifold, and heterotic string compactifications have a classical no-scale structure [5, 6, 7]. It has been shown that in Type IIB orientifold compactifications, this type of supersymmetry breaking corresponds to turning on RR and NS fluxes, which are generically present in order to cancel tadpoles as well as to stabilize closed-string moduli. Indeed, this is the case in the so-called large volume models [8] [9]. This combined with the generic appearance of the no-scale structure across many string compactifications leads to the idea that supersymmetry breaking is moduli dominated.

In string models, supersymmetry breaking is typically performed in a hidden sector as well as through the universal moduli and dilaton fields. For a given string compactification, the precise nature of the supersymmetry breaking is determined by model-dependent calculations. However,

at present there are no specific string compactifications which completely satisfy all theoretical criteria which are desired in such a model. Thus, a model-independent approach is perhaps wiser at the present time. The most studied model of supersymmetry breaking is minimal supergravity (mSUGRA), which arises from adopting the simplest ansatz for the Kähler metric, treating all chiral superfields symmetrically. In this framework,  $\mathcal{N} = 1$  supergravity is broken in a hidden sector which is communicated to the observable sector through gravitational interactions. Such models are characterized by the following parameters: a universal scalar mass  $m_0$ , a universal gaugino mass  $m_{1/2}$ , the Higgsino mixing  $\mu$ -parameter, the Higgs bilinear  $B$ -parameter, a universal trilinear coupling  $A_0$ , and  $\tan \beta$ . One then determines the  $B$  and  $|\mu|$  parameters by the minimization of the Higgs potential triggering REWSB, with the sign of  $\mu$  remaining undetermined. Thus, we are left with only four parameters. Although, this is one of the most generic frameworks that can be adopted, many string compactifications typically yield expressions for the soft terms which are even more constrained, due to the no-scale structure which emerges naturally in these theories assuming that supersymmetry breaking is dominated by the closed-string moduli. In particular, in such nSUGRA models, we will generically have  $m_0 = m_0(m_{1/2})$  and  $A = A(m_{1/2})$ . This reduces the number of free parameters compared to mSUGRA down to two,  $m_{1/2}$  and  $\tan \beta$ . In fact, adopting a strict no-scale framework, one can also fix the  $B$ -parameter as  $B = B(m_{1/2})$ , and thus we are led to a *one-parameter* model where all of the soft terms may be fixed in terms of  $m_{1/2}$ .

If we assume that the supersymmetry breaking is triggered by some of the moduli fields in a given string compactification, namely the dilaton  $S$  and the three Kähler moduli  $T$  which obtain VEVs  $\langle F_S \rangle$  and  $\langle F_T \rangle$  respectively, a simple expression for the scalar masses may be adopted:

$$\tilde{m}_i^2 = m_{3/2}^2(1 + n_i \cos^2 \theta), \quad (1)$$

with  $\tan \theta = \langle F_S \rangle / \langle F_T \rangle$  and where  $m_{3/2}$  is the gravitino mass and  $n_i$  are the modular weights of the respective matter fields.

In order to obtain universal scalar masses, which are highly suggested by the required absence of FCNC [10], there are two possible cases which may be considered: (i) setting  $\theta = \pi/2$  so that  $\langle F_S \rangle \gg \langle F_T \rangle$ ; or (ii) setting all  $n_i$  to be the same ( $n_i = -1$ ) and  $\theta = 0$  so that  $\langle F_T \rangle \gg \langle F_S \rangle$  so that all scalar masses vanish at the unification scale. The first of these two cases is referred to as the special *dilaton* scenario,

$$m_0 = \frac{1}{\sqrt{3}}m_{1/2}, \quad A = -m_{1/2}, \quad B = \frac{2}{\sqrt{3}}m_{1/2}. \quad (2)$$

while the second is referred to as the strict *moduli* scenario,

$$m_0 = 0, \quad A = 0, \quad B = 0. \quad (3)$$

For many string compactifications, especially those within the free-fermionic class of models in particular those with a flipped  $SU(5)$  gauge group [11], the soft-terms will have such a form. Interestingly, soft terms for heterotic M-theory compactifications with moduli or dilaton dominated supersymmetry breaking take the form [12]

$$\begin{aligned} m_{1/2} &= \frac{\sqrt{3}m_{3/2}}{1+x} \\ m_0^2 &= m_{3/2}^2 - \frac{3m_{3/2}^2}{(3+x)^2}x(6+x) \\ A &= -\frac{\sqrt{3}m_{3/2}}{3+x}(3-2x) \end{aligned} \quad (4)$$

which reduce to the above dilaton scenario in the limit  $x \rightarrow 0$ , where

$$x \propto \frac{(T + \overline{T})}{S + \overline{S}} \quad (5)$$

In addition, the so-called large-volume models have been studied extensively [8] [9] in recent years and the generic soft terms for this framework have been calculated in [13]. These models involve Type IIB compactifications where the moduli are stabilized by fluxes and quantum corrections to the Kähler potential generate an exponentially large volume. This exponentially large volume may lower the string scale to an intermediate level which can be in the range  $m_s \sim 10^{3-15}$  GeV. In such models, the soft terms can take the form

$$\begin{aligned} m_0 &= \frac{1}{\sqrt{3}}M \\ A_0 &= -M \\ B &= -\frac{4}{3}M \end{aligned} \quad (6)$$

where  $M$  is a universal gaugino mass, which are essentially identical to the special dilaton scenario given above. However, this framework is different from our analysis in that the string scale may be lower than what is usually taken for the grand unification scale  $\approx 2.1 \times 10^{16}$  GeV. Thus, in this scenario the observed unification of the gauge couplings when extrapolated to high energies is merely coincidental. Of course, this then also affects the running of the soft-masses resulting in different superpartner spectra than what would otherwise be obtained. More generally, no-scale type moduli-dominant scenarios of SUSY breaking are favored by F-theory [14], as are models with a flipped  $SU(5)$  gauge group [15].

Although the soft terms for wide classes of string compactifications tend to be some limit of the one-parameter model with corrections, those models constructed in Type IIA string theory with intersecting  $D6$ -branes without flux are an exception. In this case, the soft terms may exhibit complete non-universality. An analysis of the soft-terms and resulting superpartner spectra for a particular intersecting  $D6$ -brane model with desirable semi-realistic features was performed in [16].

In this work, we identify the regions of the supersymmetry parameter space for a generic one-parameter model which are allowed by current experimental constraints and explore the collider signatures which may be observed at LHC. We find that in the strict moduli scenario, there are no regions of the parameter space which may satisfy all constraints. However, for the dilaton scenario, there are small regions of the parameter space where all constraints may be satisfied and for which the observed dark matter density may be generated. The model is thus highly predictive and/or falsifiable due to its highly constrained nature. We then simulate the different collider signatures for this model which may be observed at LHC and compare to those for a intersecting  $D6$ -brane model, which possesses many desirable phenomenological characteristics. We find that there are certain signatures which may be used to discriminate between these different classes of models.

## II. PARAMETER SPACE AND SUPERPARTNER SPECTRA

The one-parameter model has been much studied in the past [17, 18, 19]. However, the last such analysis was performed some years ago. In the intervening time, the experimental constraints on SUSY models have been updated considerably, especially in regards to the constraints on the dark matter density. In addition, the experimental determination of the top quark mass has become considerably more precise in recent years. Here, we will generate a set of soft terms at the unification scale using the ansatz given in Eqs. 2 and Eqs. 3 for both the dilaton and moduli scenarios. The soft terms are then input into `MicrOMEGAs 2.0.7` [20] using `SuSpect 2.34` [21] as a front end to run the soft terms down to the electroweak scale via the Renormalization Group Equations (RGEs) and then to calculate the corresponding relic neutralino density. We take the top quark mass to be  $m_t = 171.4$  GeV and leave  $\tan \beta$  as a free parameter, while  $\mu$  is determined by the requirement of REWSB. However, we do take  $\mu > 0$  as suggested by the results of  $g_\mu - 2$  for the muon. The resulting superpartner spectra are then filtered according to the following criteria:

1. The WMAP 5-year data [22] for the cold dark matter density,  $0.1109 \leq \Omega_{\chi^0} h^2 \leq 0.1177$ . We also consider the WMAP  $2\sigma$  results [23],  $0.095 \leq \Omega_{\chi^0} h^2 \leq 0.129$ . In addition, we look at the Supercritical String Cosmology (SSC) model [24] for the dark matter density, in which

a dilution factor of  $\mathcal{O}$  is allowed [25], where  $\Omega_{\chi^o} h^2 \leq 1.1$ . For a discussion of the SSC model within the context of mSUGRA, see [26]. We investigate two cases, one where a neutralino LSP is the dominant component of the dark matter and another where it makes up a subdominant component such that  $0 \leq \Omega_{\chi^o} h^2 \leq 0.1177$ ,  $0 \leq \Omega_{\chi^o} h^2 \leq 0.129$ , and  $0 \leq \Omega_{\chi^o} h^2 \leq 1.1$ .

2. The experimental limits on the Flavor Changing Neutral Current (FCNC) process,  $b \rightarrow s\gamma$ . The results from the Heavy Flavor Averaging Group (HFAG) [27], in addition to the BABAR, Belle, and CLEO results, are:  $Br(b \rightarrow s\gamma) = (355 \pm 24_{-10}^{+9} \pm 3) \times 10^{-6}$ . There is also a more recent estimate [28] of  $Br(b \rightarrow s\gamma) = (3.15 \pm 0.23) \times 10^{-4}$ . For our analysis, we use the limits  $2.92 \times 10^{-4} \leq Br(b \rightarrow s\gamma) \leq 3.81 \times 10^{-4}$ .
3. The anomalous magnetic moment of the muon,  $g_\mu - 2$ . For this analysis we use the lower bound  $a_\mu > 11 \times 10^{-10}$  [29].
4. The process  $B_s^0 \rightarrow \mu^+ \mu^-$  where the decay has a  $\tan^6 \beta$  dependence. We take the upper bound to be  $Br(B_s^0 \rightarrow \mu^+ \mu^-) < 1.5 \times 10^{-7}$  [30].
5. The LEP limit on the lightest CP-even Higgs boson mass,  $m_h \geq 114$  GeV [31].

A scan of the full parameter space was performed for both the strict moduli scenario and the dilaton scenario. The gaugino mass  $m_{1/2}$  was varied in increments of 1 GeV in the range 50 – 2000 GeV while  $\tan\beta$  was varied in increments of 0.1 in the range 1 – 60. For the moduli scenario for  $m_{1/2}$ ,  $m_0 = 0$ ,  $A_0 = 0$ , and  $\tan\beta$  taken as a free parameter, it is found that there are no spectra which satisfy all constraints. This analysis was conducted for the strict no-scale moduli scenario only. However, solutions may be found when non-leading order corrections to the no-scale model are taken into account. For a detailed study concerning these corrections to the no-scale model, see [32]. We conclude that there are no solutions for the moduli scenario unless these corrections are incorporated, and for the present work no further study will be conducted into the strict moduli scenario for the present work.

Next, a full scan of the parameter space was performed for the dilaton scenario for  $m_{1/2}$ ,  $m_0 = \frac{1}{\sqrt{3}}m_{1/2}$ ,  $A_0 = -m_{1/2}$ , and taking  $\tan\beta$  as a free parameter. With  $m_t = 171.4$  GeV, a small region of the parameter space which satisfies all constraints is found. We exhibit the parameter space which results in a relic density satisfying the WMAP limits in Fig. 1. If the relic neutralino LSP comprises a sub-dominant component of the dark matter, we should not impose the lower bound

on the WMAP limits. Thus, the parameter space for four cases are graphed: 1)  $0.1109 \leq \Omega_{\chi^0} h^2 \leq 0.1177$ , 2)  $0.095 \leq \Omega_{\chi^0} h^2 \leq 0.129$ , 3)  $0 \leq \Omega_{\chi^0} h^2 \leq 0.1177$ , and 4)  $0 \leq \Omega_{\chi^0} h^2 \leq 0.129$ . Note that the parameter space in Fig. 1 is allowed by all constraints, except those regions noted where there is no RGE solution,  $\chi_1^0$  is not the Lightest Supersymmetric Particle (LSP), or excluded by the muon  $g_\mu - 2$  results. The regions enclosed by the dashed lines are within the WMAP limits. Fig. 2 displays the parameter space allowed by all constraints for the SSC model of the dark matter density. The WMAP region is the small thin region at the top. The shaded area below the WMAP region is allowed by all constraints, though  $0.129 < \Omega_{\chi^0} h^2 \leq 1.1$ . The cross-hatched region is allowed by all constraints, though  $\Omega_{\chi^0} h^2 > 1.1$ . The region excluded by  $m_h < 114$  GeV satisfies all other constraints, including  $\Omega_{\chi^0} h^2 \leq 1.1$ . The remaining regions are excluded for the reasons noted on the plot.

Imposing all the experimental constraints, we find that the viable WMAP parameter space is in the range  $\tan\beta = 35.5$  to  $\tan\beta = 38$  as shown in Fig. 1. Extending the dark matter density to the SSC model in Fig. 2, the allowed parameter space expands from  $\tan\beta = 10.2$  to  $\tan\beta = 38$ . We show in Table I the allowed ranges for the CP-even Higgs boson mass satisfying all constraints for each range of  $\Omega_{\chi^0} h^2$  within the parameter space. As we see, the higgs mass is highly constrained in each of the cases. A histogram plot of all the higgs masses for each superpartner spectra allowed by the constraints are shown in Fig. 3 for each of the four WMAP cases of the dark matter density ranges we consider. The width of each bin is 0.05 GeV, and all plots are normalized so that the height of each bin represents the frequency of occurrence of the higgs mass falling within that 0.05 GeV range. Fig. 4 is a similar higgs histogram plot for  $0 \leq \Omega_{\chi^0} h^2 \leq 1.1$  with the same 0.05 GeV bin width.

For the superpartner spectra allowed by the constraints, there are only two mass patterns. Both are stau patterns: 1)  $\tilde{\chi}_1^0 < \tilde{\tau} < \tilde{e}_R < \tilde{\chi}_1^\pm$ , and 2)  $\tilde{\chi}_1^0 < \tilde{\tau} < \tilde{e}_R < \tilde{\nu}_\tau$ . A characteristic of the coannihilation region is the nearly degenerate mass of the lightest neutralino and the stau, which is in fact what we find for these spectra in the WMAP region. We also discover all LSP allowed by the constraints are Bino.

### III. SIGNATURES AT THE LHC

In this section, we discuss the collider signatures of the one-parameter model which may be observed at LHC. To simulate events for different regions of the allowed parameter space, the superpartner mass spectra are first calculated using `SuSpect` 2.34. Then production cross-sections

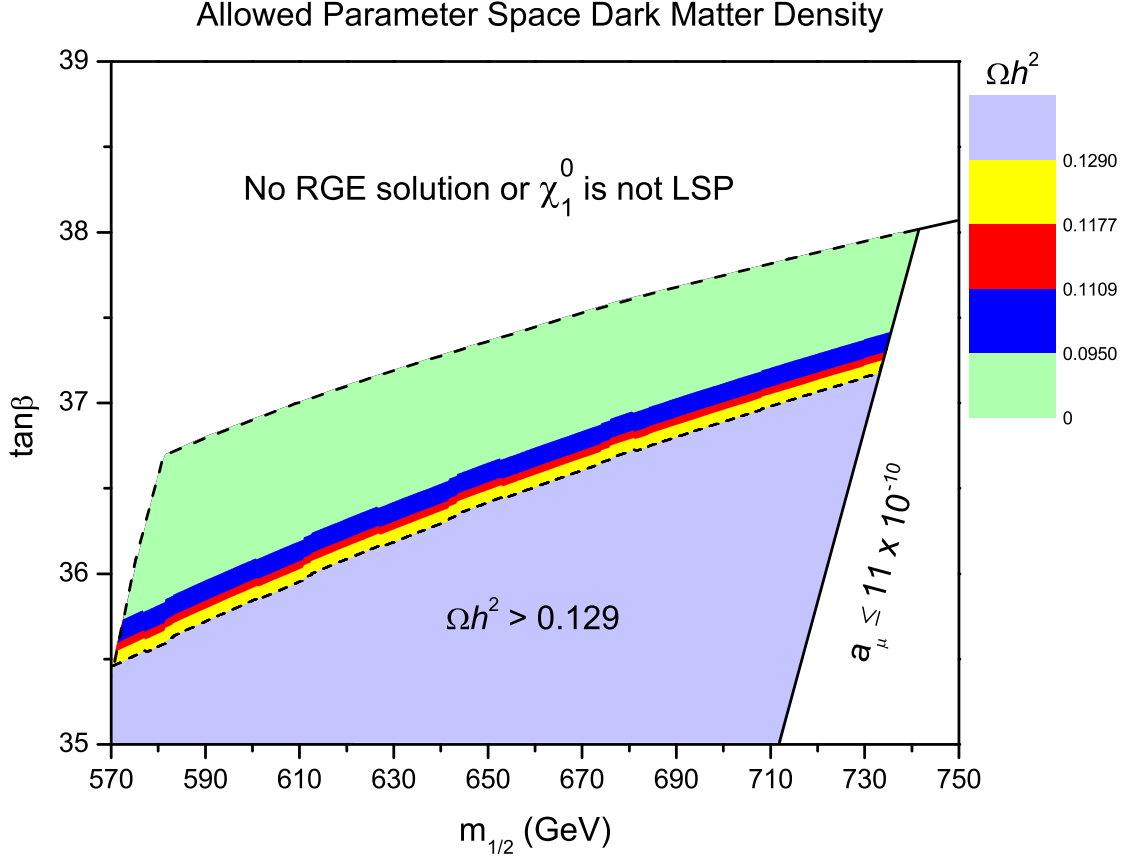


FIG. 1: Parameter space allowed by all constraints. The WMAP region is enclosed by the dashed lines. The shaded area below the WMAP region is allowed by all constraints, though  $0.129 < \Omega_{\chi^0} h^2 \leq 1.1$ . The region on the far right side of the plot is excluded by the  $g_\mu - 2$  results. The remaining area is excluded for the reasons noted.

and branching ratios are calculated using PYTHIA 6.4.14 [33]. The simulated events are then generated using the code PGS4 [34]. A SUSY Le Houches Accord (SLHA) [35] file is output by Suspect 2.34 and this SLHA file is then called by PYTHIA via PGS4. In the PYTHIA card file, MSEL = 39 is used to generate 91 Minimal Symmetric Standard Model (MSSM)  $2 \rightarrow 2$  production processes, excluding only single higgs production. The default configuration of the LHC Detector Card and the Level 1 (L1) trigger are used in PGS4. The L1 trigger values are close to the actual values used by the Compact Muon Solenoid Detector (CMS) experiment. A table of the L1 trigger values can be found here [36]. A total integrated luminosity of  $10 \text{ fb}^{-1}$  of data was simulated for all signatures. This corresponds to approximately one to two years of data collection at LHC. At this point, master cuts above and beyond the L1 trigger values can be applied to streamline the



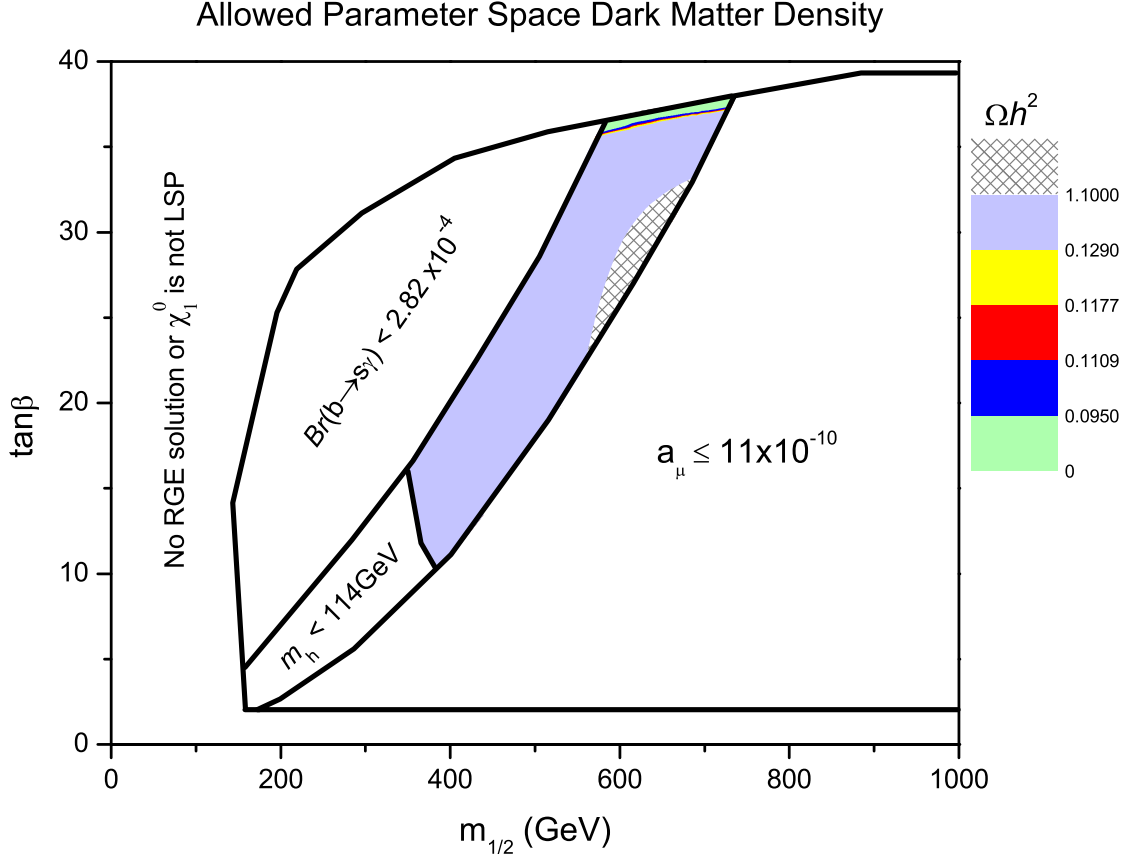


FIG. 2: Parameter space allowed by all constraints for the SSC model. The WMAP region is the small thin region at the top. The shaded area below the WMAP region is allowed by all constraints, though  $0.129 < \Omega_{\chi^0} h^2 \leq 1.1$ . The region excluded by  $m_h < 114 \text{ GeV}$  satisfies all other constraints, including  $\Omega_{\chi^0} h^2 \leq 1.1$ . The remaining areas are excluded for the reasons noted.

data even further. To apply master cuts and count collider observables, the program Chameleon Root (ChRoot) [37] was used. The master cuts used for the one-parameter model are

- $P_T > 60 \text{ GeV}$  and  $|\eta| < 3$  for jets
- $P_T > 20 \text{ GeV}$  and  $|\eta| < 2.4$  for photons and leptons
- $P_T^{miss} > 215 \text{ GeV}$  for missing transverse momentum.

These same master cuts are also applied to the Standard Model (SM) background. Constructing an estimate of the SM background is a nontrivial task. The technical difficulty involves the number of background events. The number of background events is so much larger than the signal that

TABLE I: Allowed ranges of the CP-even Higgs boson mass (in GeV) which satisfy the WMAP and SSC dark matter density limits as well as all other constraints.

$\Omega_{\chi^0} h^2$	$m_h$ (GeV)
$0.1109 \leq \Omega_{\chi^0} h^2 \leq 0.1177$	117.17 - 118.58
$0.095 \leq \Omega_{\chi^0} h^2 \leq 0.129$	117.16 - 118.60
$0 \leq \Omega_{\chi^0} h^2 \leq 0.1177$	117.17 - 118.64
$0 \leq \Omega_{\chi^0} h^2 \leq 0.129$	117.16 - 118.64
$0 \leq \Omega_{\chi^0} h^2 \leq 1.1$	114.00 - 118.64

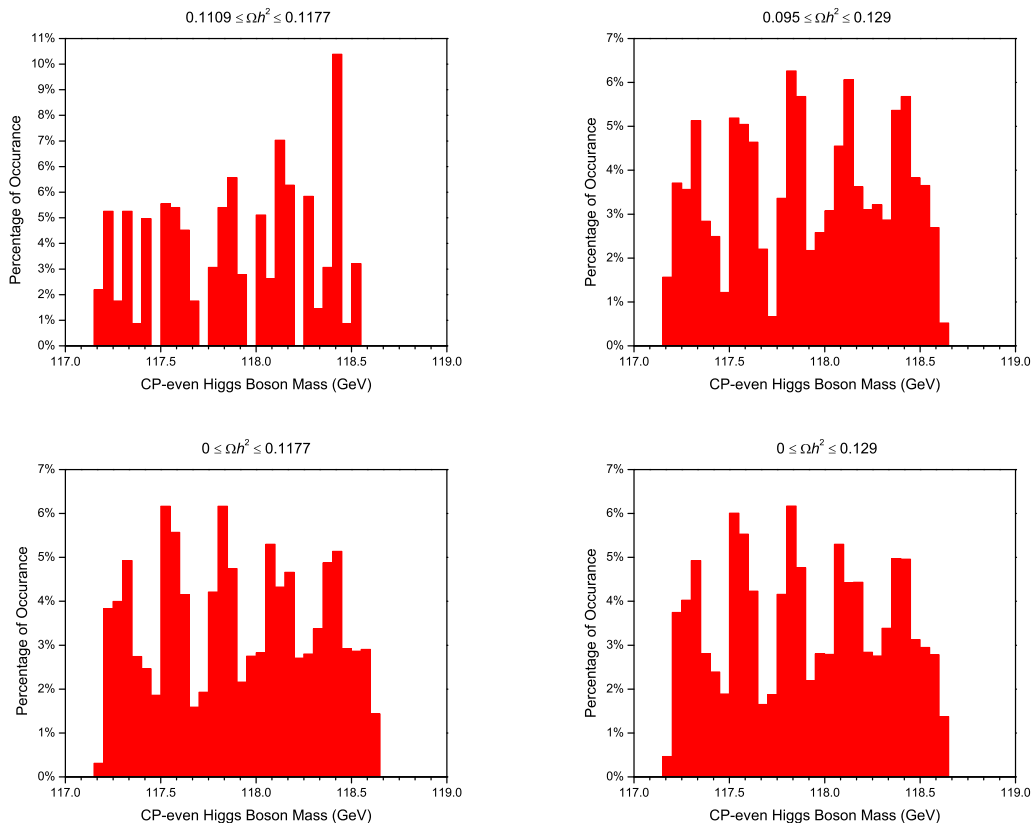


FIG. 3: Histogram plots of all higgs masses of all spectra allowed by the constraints for each of the WMAP dark matter density ranges. Each bin width is 0.05 GeV and this plot has been normalized so that the height of each bin represents the frequency of occurrence of the higgs mass falling within that 0.05 GeV range.

most SM events must be discarded in the interest of compute time. Another major issue concerns simulating the largest component of the SM background, QCD physics. The simulation of W-bosons, quarks, and gluons is very problematic. In the interest of reducing the compute time as much as possible, we use the SM background sample on the LHC Olympics website [38]. This

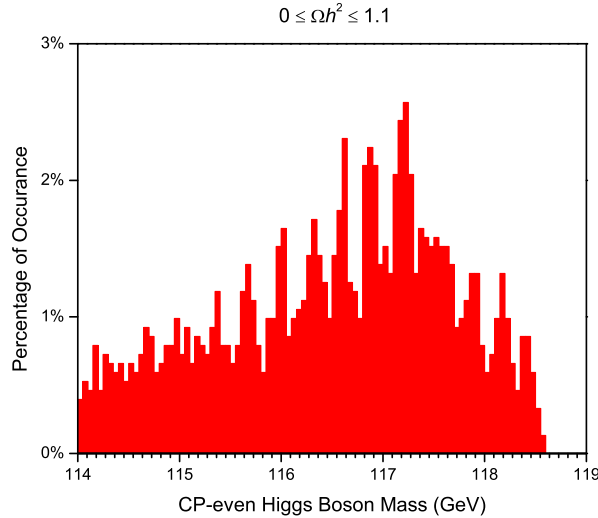


FIG. 4: Histogram plot of all higgs masses of all spectra allowed by the constraints for the SSC model with  $0 \leq \Omega_{\chi} h^2 \leq 1.1$ . Each bin width is 0.05 GeV and this plot has been normalized so that the height of each bin represents the frequency of occurrence of the higgs mass falling within that 0.05 GeV range.

background sample was used for the LHC Olympics and contains  $5 \text{ fb}^{-1}$  of LHC SM background data. We utilize this sample to formulate an estimate of the SM background for an integrated luminosity of  $10 \text{ fb}^{-1}$  of detector data. This SM background sample contains dijets,  $t\bar{t}$ , and W/Z+jets processes. To determine if a signal is observable above the SM background, an inclusive count of the individual signatures in the signal is compared to a count of the individual signatures in the background. In order for a signature to be observable above the background, the following requirements must be satisfied [39]:

$$\frac{S}{\sqrt{B}} > 4, \quad S > 5$$

where S is the number of signal events and B is the number of background events that survive the master cuts and any additional cuts. An estimate of the observable limit due to the SM background can be computed and compared to the MSSM production process number of events for each signature in order to determine whether a particular signature is observable above the background after the cuts have been applied. In our analysis, the signal is composed of 43 different signatures involving leptons (e,  $\mu$ , and  $\tau$ , unless noted otherwise), jets, and b-tagged jets. The total number of events per  $10 \text{ fb}^{-1}$  LHC data are counted and graphed. The following abbreviations are used in describing the signatures: Same Sign (SS), Opposite Sign (OS), Same Flavor (SF), and Different Flavor (DF). Some of these signatures have been used in other analyses [39] [40]. The

signatures studied are:

- 1 lepton, OS dilepton, SS dilepton, trilepton, 1 tau lepton, 2 tau leptons, 3 tau leptons, OSSF dilepton, OSDF dilepton, SSSF dilepton, SSDF dilepton, OS dilepton( $e,\mu$ ), SS dilepton( $e,\mu$ )
- 1 jet, 2 jets, 3 jets, 4 jets, 1 b-jet, 2 b-jets, 3 b-jets, 4 b-jets
- 2 leptons and 1 jet, 2 leptons and 2 jets, 2 leptons and 3 jets, 2 leptons and 4 jets
- 0 leptons and 2 b-jets, 0 leptons and  $\geq 3$  b-jets, 1 lepton and  $\geq 2$  b-jets, 2 leptons and 0 b-jets, 2 leptons and 1 b-jet, 2 leptons and 2 b-jets, 2 leptons and  $\geq 3$  b-jets, 3 leptons and 1 b-jet
- 1 tau and  $\geq 1$  b-jet, 1 tau and  $\geq 2$  b-jets, 2 tau and  $\geq 2$  b-jets, 2 tau and  $\geq 1$  b-jet
- 2 leptons and  $\geq 2$  jets, 3 leptons and  $\geq 2$  jets, OS 2 tau and  $\geq 2$  jets
- 1 positive lepton, 1 negative lepton, clean dilepton

We examine these signatures in two distinctive formats. First, we present the signatures for the one-parameter model in isolation, displaying the number of events per  $10\text{ fb}^{-1}$  LHC data for each of the 43 signatures studied. These plots provide a general illustration of the one-parameter model collider signatures and correlate the number of events for each signature to the observable limit due to the Standard Model background computed for specific cuts. Concluding this paper, we present a comparison of significant signatures of the one-parameter model versus an alternative string compactification model, attempting to use collider signatures to distinguish between these two models.

Fig. 5 exhibits the signatures for two spectra within the WMAP region allowed by all constraints as shown in Fig 1. The low energy supersymmetric particles and masses for the spectra represented in Fig. 5 are shown in Table II and Table III. The varying solid black line in the plot represents the observable limit computed in accordance with the requirements stated in this section due to the Standard Model background and based upon the specified cuts. Fig. 6 is a similar plot, though we don't impose a lower bound on the dark matter density. The low energy supersymmetric particles and masses for the spectra represented in Fig. 6 are shown in Table IV, Table V, and Table VI. Fig. 7 displays the number of events for the SSC dark matter density model. One spectrum for each  $\tan\beta$  allowed by the constraints was simulated in the event generator and graphed in Fig. 7. The details of the spectra in this plot are listed in Table VII. The bar chart in Fig. 8 provides a more clear picture of how many signatures in Fig. 7 are observable for each  $\tan\beta$  for the master

TABLE II: Low energy supersymmetric particles and their masses (in GeV) for  $m_{1/2} = 606$ ,  $m_0 = 349.9$ ,  $A_0 = -606$ ,  $\tan\beta = 36$ ,  $\mu > 0$ ,  $\Omega_{\chi^0} h^2 = 0.1147$  simulated in event generator in Fig. 5.

$h^0$	$H^0$	$A^0$	$H^\pm$	$\tilde{g}$	$\chi_1^\pm$	$\chi_2^\pm$	$\chi_1^0$	$\chi_2^0$
117.6	753.9	753.9	758.4	1377	482.9	840.8	254.1	483.0
$\chi_3^0$	$\chi_4^0$	$\tilde{t}_1$	$\tilde{t}_2$	$\tilde{u}_1/\tilde{c}_1$	$\tilde{u}_2/\tilde{c}_2$	$\tilde{b}_1$	$\tilde{b}_2$	
832.4	840.4	932.6	1169	1251	1294	1109	1174	
$\tilde{d}_1/\tilde{s}_1$	$\tilde{d}_2/\tilde{s}_2$	$\tilde{\tau}_1$	$\tilde{\tau}_2$	$\tilde{\nu}_\tau$	$\tilde{e}_1/\tilde{\mu}_1$	$\tilde{e}_2/\tilde{\mu}_2$	$\tilde{\nu}_e/\tilde{\nu}_\mu$	<i>LSP</i>
1246	1297	263.2	509.3	485.2	416.5	532.8	527.0	<i>Bino</i>

TABLE III: Low energy supersymmetric particles and their masses (in GeV) for  $m_{1/2} = 702$ ,  $m_0 = 405.3$ ,  $A_0 = -702$ ,  $\tan\beta = 37$ ,  $\mu > 0$ ,  $\Omega_{\chi^0} h^2 = 0.1143$  simulated in event generator in Fig. 5.

$h^0$	$H^0$	$A^0$	$H^\pm$	$\tilde{g}$	$\chi_1^\pm$	$\chi_2^\pm$	$\chi_1^0$	$\chi_2^0$
118.4	849.3	849.3	853.3	1578	562.9	956.1	296.5	563.0
$\chi_3^0$	$\chi_4^0$	$\tilde{t}_1$	$\tilde{t}_2$	$\tilde{u}_1/\tilde{c}_1$	$\tilde{u}_2/\tilde{c}_2$	$\tilde{b}_1$	$\tilde{b}_2$	
948.5	955.8	1075	1325	1432	1483	1269	1335	
$\tilde{d}_1/\tilde{s}_1$	$\tilde{d}_2/\tilde{s}_2$	$\tilde{\tau}_1$	$\tilde{\tau}_2$	$\tilde{\nu}_\tau$	$\tilde{e}_1/\tilde{\mu}_1$	$\tilde{e}_2/\tilde{\mu}_2$	$\tilde{\nu}_e/\tilde{\nu}_\mu$	<i>LSP</i>
1426	1485	304.6	581.8	560.2	481.6	615.6	610.6	<i>Bino</i>

cuts and additional cuts used to generate Fig. 7. The  $\tan\beta$  with the largest range of dark matter density for the SSC model is  $\tan\beta = 34$ , thus, we plot signatures for  $\tan\beta = 34$  in Fig. 9 for various values of the dark matter density. The low energy supersymmetric particles and masses of the spectra in this plot are listed in Table VIII. Fig. 10 shows the number of signatures in Fig. 9 that are observable for each value of the dark matter density for the master cuts and additional cuts used to construct Fig. 9. Since we are examining the one-parameter model exclusively in Fig. 5, Fig. 6, Fig. 7, and Fig. 9, we make an additional cut of  $P_T^{miss} > 275$  GeV over and above the master cut of  $P_T^{miss} > 215$  GeV for missing transverse momentum in these four plots only. All other master cuts remain unchanged.

#### IV. SPARTICLE PRODUCTION AND DECAY

In a one-parameter model universe, predominantly squarks and gluinos will be produced at LHC. The cross-sections for the one-parameter model were calculated with PYTHIA for  $\tan\beta$  allowed by the constraints. In general, all  $\tan\beta$  allowed by the constraints had similar dominant cross-sections. The dominant SUSY cross sections for the dilaton scenario at LHC are given by:

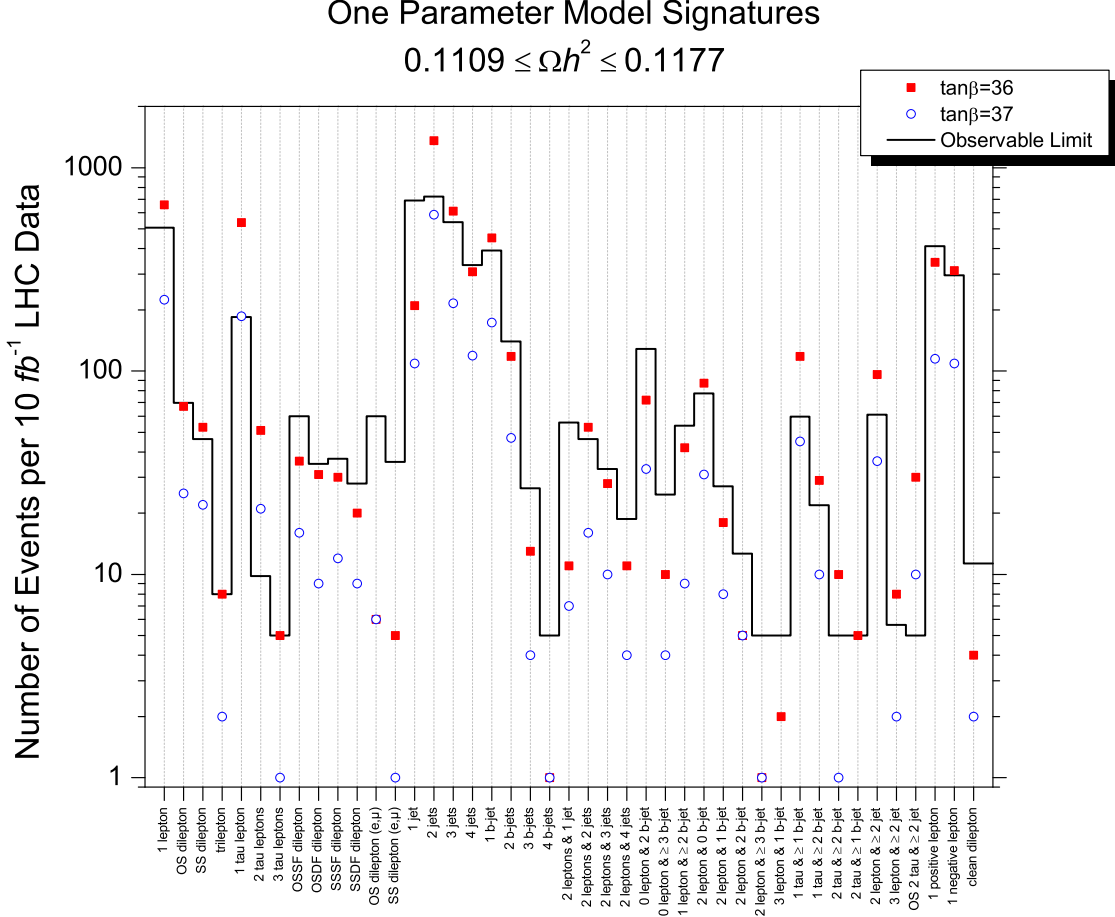


FIG. 5: Signatures of superpartner spectra within WMAP region. Spectra in this plot are listed in Table II and Table III. The solid bold line represents the observable limit computed in accordance with the requirements in Section III due to the Standard Model background. The markers represent the number of events per  $10 \text{ fb}^{-1}$  LHC data. An additional cut of  $P_T^{miss} > 275 \text{ GeV}$  was applied in this plot.

$$q_i + q_j \rightarrow \tilde{q}_{iR} + \tilde{q}_{jR}$$

$$q_i + q_j \rightarrow \tilde{q}_{iL} + \tilde{q}_{jL}$$

$$q_i + q_j \rightarrow \tilde{q}_{iL} + \tilde{q}_{jR}$$

$$q_j + g \rightarrow \tilde{q}_{jL} + \tilde{g}$$

$$q_j + g \rightarrow \tilde{q}_{jR} + \tilde{g}$$

$$q_i + \bar{q}_j \rightarrow \tilde{q}_{iL} + \tilde{\bar{q}}_{jR}$$

$$q_i + \bar{q}_j \rightarrow \tilde{q}_{iR} + \tilde{\bar{q}}_{jR}$$

These seven processes have the largest cross-sections and will be a major source for squarks and gluinos. We present squark and gluino decay processes that result in observed LHC signatures and provide branching ratios for these processes. The branching ratio listed will be the range over  $\tan\beta$ ,

TABLE IV: Low energy supersymmetric particles and their masses (in GeV) for  $m_{1/2} = 590$ ,  $m_0 = 340.6$ ,  $A_0 = -590$ ,  $\tan\beta = 36$ ,  $\mu > 0$ ,  $\Omega_{\chi^0} h^2 = 0.0901$  simulated in event generator in Fig. 6.

$h^0$	$H^0$	$A^0$	$H^\pm$	$\tilde{g}$	$\chi_1^\pm$	$\chi_2^\pm$	$\chi_1^0$	$\chi_2^0$
117.3	734.7	734.7	739.3	1342	469.6	819.6	247.2	469.7
$\chi_3^0$	$\chi_4^0$	$\tilde{t}_1$	$\tilde{t}_2$	$\tilde{u}_1/\tilde{c}_1$	$\tilde{u}_2/\tilde{c}_2$	$\tilde{b}_1$	$\tilde{b}_2$	
811.0	819.2	907.2	1141	1219	1261	1079.4	1144	
$\tilde{d}_1/\tilde{s}_1$	$\tilde{d}_2/\tilde{s}_2$	$\tilde{\tau}_1$	$\tilde{\tau}_2$	$\tilde{\nu}_\tau$	$\tilde{e}_1/\tilde{\mu}_1$	$\tilde{e}_2/\tilde{\mu}_2$	$\tilde{\nu}_e/\tilde{\nu}_\mu$	$LSP$
1214	1263	254.7	496.9	472.2	405.6	518.9	513.0	$Bino$

TABLE V: Low energy supersymmetric particles and their masses (in GeV) for  $m_{1/2} = 650$ ,  $m_0 = 375.3$ ,  $A_0 = -650$ ,  $\tan\beta = 37$ ,  $\mu > 0$ ,  $\Omega_{\chi^0} h^2 = 0.0559$  simulated in event generator in Fig. 6.

$h^0$	$H^0$	$A^0$	$H^\pm$	$\tilde{g}$	$\chi_1^\pm$	$\chi_2^\pm$	$\chi_1^0$	$\chi_2^0$
117.9	803.6	803.6	807.8	1468	519.7	891.5	273.7	519.7
$\chi_3^0$	$\chi_4^0$	$\tilde{t}_1$	$\tilde{t}_2$	$\tilde{u}_1/\tilde{c}_1$	$\tilde{u}_2/\tilde{c}_2$	$\tilde{b}_1$	$\tilde{b}_2$	
883.4	891.2	996.3	1238	1332	1379	1179	1244	
$\tilde{d}_1/\tilde{s}_1$	$\tilde{d}_2/\tilde{s}_2$	$\tilde{\tau}_1$	$\tilde{\tau}_2$	$\tilde{\nu}_\tau$	$\tilde{e}_1/\tilde{\mu}_1$	$\tilde{e}_2/\tilde{\mu}_2$	$\tilde{\nu}_e/\tilde{\nu}_\mu$	$LSP$
1327	1381	277.5	541.7	518.4	446.3	570.7	565.3	$Bino$

unless the ratio varies by less than 1%. Table IX lists the branching ratios for the squark decays, and Table X lists the branching ratios for neutralino, chargino, gluino, stop, top, stau, and  $W^+$  decays. The lepton, dilepton, and trilepton signatures include observable events. These signatures in the one-parameter model are primarily the consequence of squark and gluino decays.

The processes and branching ratios listed in Table IX and Table X define decays that result in lepton signatures at LHC. Lepton signatures result from various possibilities; listed below are cascade decays using processes given in Table IX and Table X:

$$\begin{aligned}
\tilde{q}_R &\rightarrow q\tilde{\chi}_2^- \rightarrow q\tilde{\tau}_1^- \nu_\tau \rightarrow q\nu_\tau \tilde{\chi}_1^0 \tau^- \\
&\tilde{q}_R \rightarrow q\tilde{\chi}_1^0 \\
\tilde{q}_R &\rightarrow b\tilde{\chi}_1^+ \rightarrow b\tilde{\tau}_1^+ \nu_\tau \rightarrow b\nu_\tau \tilde{\chi}_1^0 \tau^+ \\
\tilde{q}_L &\rightarrow q\tilde{\chi}_1^\pm \rightarrow q\tilde{\tau}_1^\pm \nu_\tau \rightarrow q\nu_\tau \tilde{\chi}_1^0 \tau^\pm \\
\tilde{q}_L &\rightarrow q\tilde{\chi}_2^0 \rightarrow q\tilde{\tau}_1^\mp \tau^\pm \rightarrow q\tau^\pm \tilde{\chi}_1^0 \tau^\mp \\
\tilde{g} &\rightarrow \tilde{t}_1 \bar{t} \rightarrow t\tilde{\chi}_1^0 \bar{b} W^- \rightarrow \tilde{\chi}_1^0 b W^+ \bar{b} d \bar{u} \rightarrow \tilde{\chi}_1^0 b \bar{s} c \bar{b} d \bar{u} \\
\tilde{g} &\rightarrow \tilde{t}_1 \bar{t} \rightarrow t\tilde{\chi}_1^0 \bar{b} W^- \rightarrow \tilde{\chi}_1^0 b W^+ \bar{b} e^- \bar{\nu}_e \rightarrow \tilde{\chi}_1^0 b \mu^+ \nu_\mu \bar{b} e^- \bar{\nu}_e
\end{aligned}$$

TABLE VI: Low energy supersymmetric particles and their masses (in GeV) for  $m_{1/2} = 738$ ,  $m_0 = 426.1$ ,  $A_0 = -738$ ,  $\tan\beta = 38$ ,  $\mu > 0$ ,  $\Omega_{\chi^0} h^2 = 0.0333$  simulated in event generator in Fig. 6.

$h^0$	$H^0$	$A^0$	$H^\pm$	$\tilde{g}$	$\chi_1^\pm$	$\chi_2^\pm$	$\chi_1^0$	$\chi_2^0$
118.55	871.69	871.69	875.62	1650	593.3	995.3	313.0	593.3
$\chi_3^0$	$\chi_4^0$	$\tilde{t}_1$	$\tilde{t}_2$	$\tilde{u}_1/\tilde{c}_1$	$\tilde{u}_2/\tilde{c}_2$	$\tilde{b}_1$	$\tilde{b}_2$	
987.8	995.0	1125	1379	1496	1549	1323	1390	
$\tilde{d}_1/\tilde{s}_1$	$\tilde{d}_2/\tilde{s}_2$	$\tilde{\tau}_1$	$\tilde{\tau}_2$	$\tilde{\nu}_\tau$	$\tilde{e}_1/\tilde{\mu}_1$	$\tilde{e}_2/\tilde{\mu}_2$	$\tilde{\nu}_e/\tilde{\nu}_\mu$	$LSP$
1490	1551	313.1	607.5	586.3	506.0	646.4	641.7	<i>Bino</i>

## V. GENERIC OPM VS. INTERSECTING $D6$ -BRANES

Much of the older work towards constructing semi-realistic string vacua was done in the context of heterotic strings. In particular, many of the most phenomenologically interesting models were those constructed within the free-fermionic formulation [11], and it is really from these types of models that the one-parameter model was first defined [17, 18, 19]. As we have pointed out in the Introduction, the same basic structure of the one-parameter model also arises in the context of heterotic M-theory constructions as well as Type IIB orientifold flux compactifications. Besides these types of string vacua, there are also Type IIA compactifications involving  $D6$ -branes intersecting at angles which have been much studied in recent years. The soft terms for intersecting  $D6$ -branes are in general non-universal, in contrast in the one-parameter model as well as the standard framework, mSUGRA. Thus, it is an interesting question whether or not it is possible to distinguish between these two different types of string compactifications.

In ref. [16] an explicit example of a supersymmetric intersecting  $D6$ -brane model in Type IIA string theory was constructed which possesses many desirable phenomenological properties. In particular, the model has three generations of SM fermions and also exhibits automatic gauge coupling unification. In addition, it is possible to obtain correct masses and mixings for both up and down-type quarks as well as the tau lepton. The soft supersymmetry breaking terms were also calculated for this model, and it was shown that there are regions within the parameter space which may generate the observed dark matter density and superpartner spectra satisfying all presently known constraints. Given the desirable phenomenology of this model, it provides a suitable candidate with which to compare the one-parameter model. In particular, the question that we would like to address is if it is possible to discriminate between this class of string vacua constructed with intersecting  $D6$ -branes in Type IIA and those models which arise in weakly-



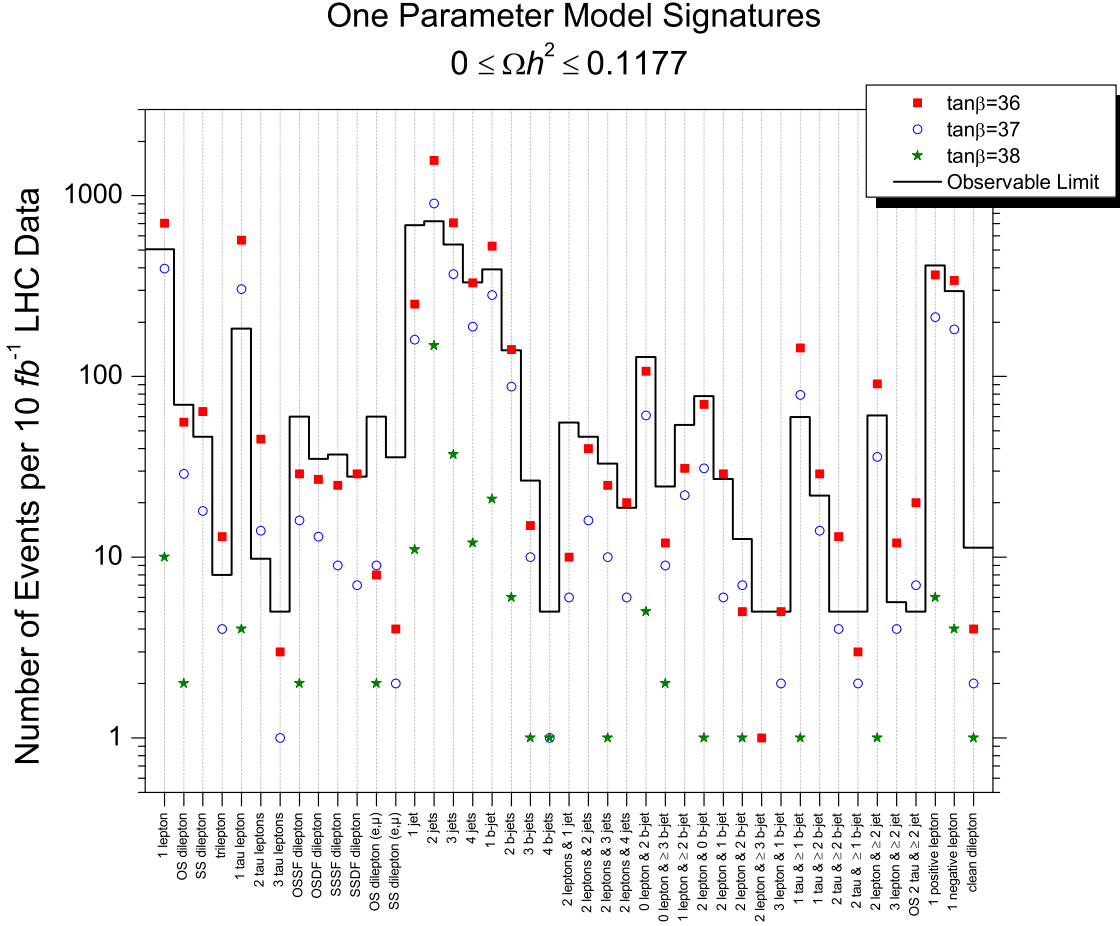


FIG. 6: Signatures of superpartner spectra within WMAP region without imposing a lower bound on the dark matter density. Spectra in this plot are listed in Table IV, Table V, and Table VI. The solid bold line represents the observable limit computed in accordance with the requirements in Section III due to the Standard Model background. The markers represent the number of events per  $10 \text{ fb}^{-1}$  LHC data. An additional cut of  $P_T^{miss} > 275 \text{ GeV}$  was applied in this plot.

coupled heterotic string theory in the collider signatures which may be observed at LHC.

In Figs. 11, 12, 13, 14, 15, 16, and 17 we plot two collider signatures against each other for both the intersecting  $D6$ -brane model and the one-parameter model. For each of the cases shown, there seems to be a clear separation between the one-parameter model and the intersecting  $D6$ -brane model. All spectra simulated in these figures from both models are within the WMAP region of the allowed parameter space. Namely, 31 spectra from the one-parameter model and 35 spectra from the intersecting  $D6$ -brane model were simulated in the event generator. Table XI lists the different mass patterns of the one-parameter model and intersecting  $D6$ -brane model. The mass patterns of the 35 superpartner spectra for the intersecting  $D6$ -brane model simulated in the event generator

TABLE VII: Superpartner spectra (in GeV) simulated in event generator in Fig. 7 for  $0 \leq \Omega_{\chi^0} h^2 \leq 1.1$ .  
 $\Delta M \equiv m_{\tilde{\tau}_1} - m_{\tilde{\chi}_1^0}$ .

$m_{1/2}$	$m_0$	$A_0$	$\tan\beta$	$Sgn\mu$	$\Omega_{\chi^0} h^2$	$m_h$	$m_{\tilde{\chi}_1^0}$	$m_{\tilde{\tau}_1}$	$\Delta M$	$m_{\tilde{g}}$	$LSP$
385	222.3	-385	11	+	0.6195	114.22	156.3	254.5	98.2	907.2	<i>Bino</i>
390	225.2	-390	12	+	0.6296	114.34	158.7	255.7	97.0	916.3	<i>Bino</i>
415	239.6	-415	13	+	0.6983	114.94	169.6	270.0	100.4	971.3	<i>Bino</i>
425	245.4	-425	14	+	0.7200	115.20	174.1	274.0	99.9	991.8	<i>Bino</i>
435	251.1	-435	15	+	0.7440	115.40	178.4	277.8	99.4	1014.3	<i>Bino</i>
450	259.8	-450	16	+	0.7840	115.65	185.0	284.7	99.7	1045.9	<i>Bino</i>
460	265.6	-460	17	+	0.8087	115.91	189.3	287.9	98.6	1068.6	<i>Bino</i>
475	274.2	-475	18	+	0.8496	116.11	196.0	294.3	98.3	1100.0	<i>Bino</i>
500	288.7	-500	19	+	0.9262	116.47	206.9	306.7	99.8	1153.5	<i>Bino</i>
510	294.4	-510	20	+	0.9508	115.66	211.2	309.0	97.8	1175.8	<i>Bino</i>
530	306.0	-530	21	+	1.0108	116.88	220.0	317.5	97.5	1217.7	<i>Bino</i>
540	311.8	-540	22	+	1.0333	116.94	224.6	319.4	94.8	1237.3	<i>Bino</i>
545	314.7	-545	23	+	1.0367	117.02	226.8	317.6	90.8	1248.3	<i>Bino</i>
550	317.5	-550	24	+	1.0386	117.10	229.0	315.6	86.6	1259.3	<i>Bino</i>
555	320.4	-555	25	+	1.0389	117.21	231.2	313.2	82.0	1270.8	<i>Bino</i>
560	323.3	-560	26	+	1.0366	117.15	233.7	310.8	77.1	1278.8	<i>Bino</i>
565	326.2	-565	27	+	1.0326	117.20	235.8	307.8	72.0	1289.6	<i>Bino</i>
570	329.1	-570	28	+	1.0251	117.30	238.0	304.5	66.5	1301.0	<i>Bino</i>
580	334.9	-580	29	+	1.0315	117.44	242.3	303.8	61.5	1323.0	<i>Bino</i>
590	340.6	-590	30	+	1.0280	117.46	247.0	302.9	55.9	1342.2	<i>Bino</i>
605	349.3	-605	31	+	1.0292	117.64	253.4	304.2	50.8	1375.1	<i>Bino</i>
620	358.0	-620	32	+	1.0011	117.72	260.3	305.3	45.0	1405.1	<i>Bino</i>
640	369.5	-640	33	+	0.9428	117.99	268.9	308.2	39.3	1449.5	<i>Bino</i>
670	386.8	-670	34	+	0.8503	118.23	282.2	316.2	34.0	1512.0	<i>Bino</i>
690	398.4	-690	35	+	0.6280	118.33	291.3	318.1	26.8	1552.3	<i>Bino</i>
700	404.1	-700	36	+	0.3361	118.41	295.6	313.7	18.1	1574.1	<i>Bino</i>
710	409.9	-710	37	+	0.1260	118.39	300.4	309.1	8.7	1592.5	<i>Bino</i>
738	426.1	-738	38	+	0.0333	118.55	313.0	313.1	0.1	1649.8	<i>Bino</i>

are the *ID6BraneP1* chargino pattern. This is in contrast to the two different stau patterns of the one-parameter model, *OPMP1* and *OPMP2*. The 31 one-parameter model spectra simulated in the event generator were a combination of both the *OPMP1* and *OPMP2* stau mass patterns. The relative mass of the stau is larger in the chargino pattern than in the stau pattern, hence a higher percentage of stau versus overall SUSY events will be produced at LHC for the stau pattern. Since

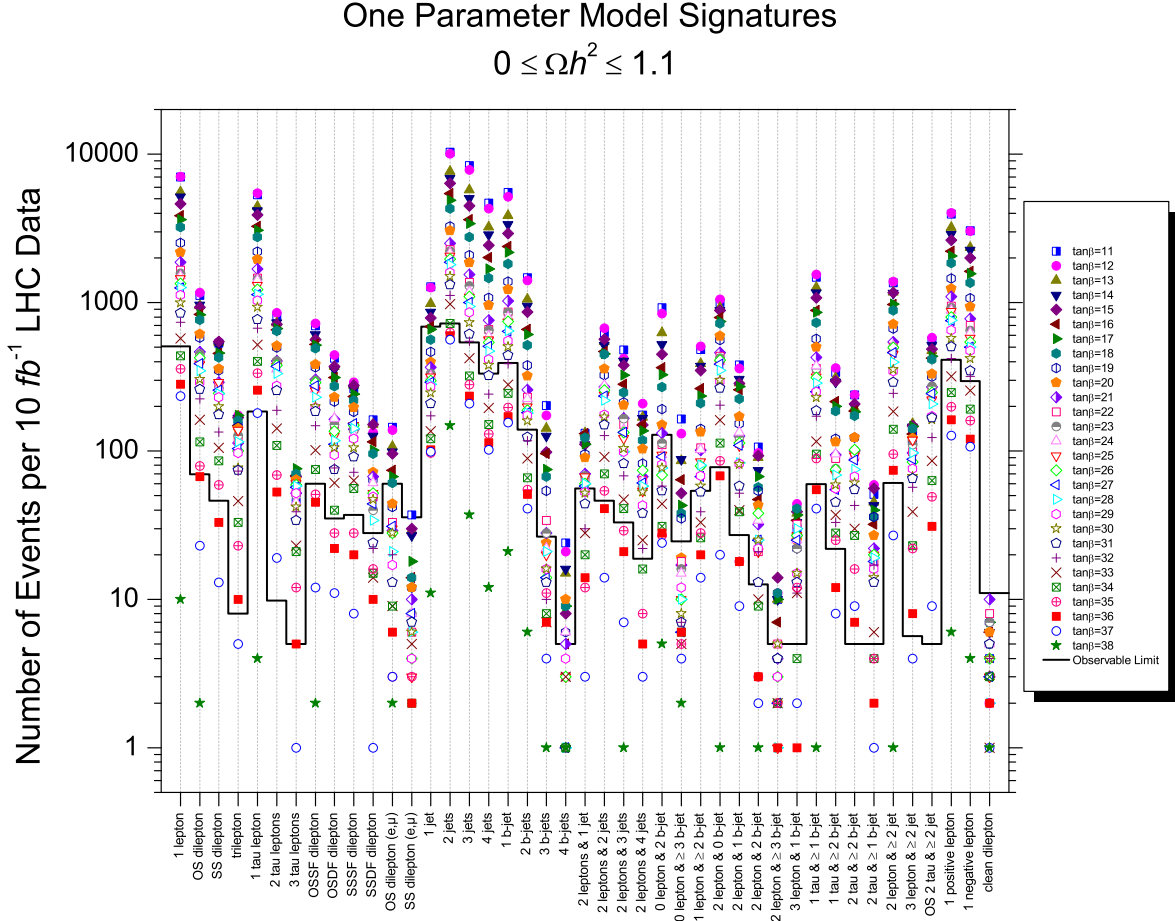


FIG. 7: Signatures of superpartner spectra for SSC. Spectra in this plot are listed in Table VII. The solid bold line represents the observable limit computed in accordance with the requirements in Section III due to the Standard Model background. The markers represent the number of events per  $10 \text{ fb}^{-1}$  LHC data. An additional cut of  $P_T^{miss} > 275 \text{ GeV}$  was applied in this plot. The number of observable signatures for each spectrum in this plot are shown in Fig. 8.

stau decay to tau 100% of the time via  $\tilde{\tau}_1^\pm \rightarrow \tilde{\chi}_1^0 \tau^\pm$ , more tau will be produced at LHC as a percentage of leptons for the one-parameter model than for the intersecting  $D6$ -brane model. This is in fact what we see in the plots of one collider signature versus another. Thus, it may be possible to discriminate between two different classes of string compactifications via the collider signatures which are observed at LHC. Though the number of tau as a percentage of leptons produced at LHC for the intersecting  $D6$ -brane chargino pattern  $ID6BraneP2$  in Table XI will increase over chargino pattern  $ID6BraneP1$ , Fig. 11 through Fig. 17 should still show discrimination when plotting the intersecting  $D6$ -brane chargino pattern  $ID6BraneP2$  versus the two one-parameter model stau patterns  $OPMP1$  and  $OPMP2$ . We reserve a more in-depth study of these additional intersecting

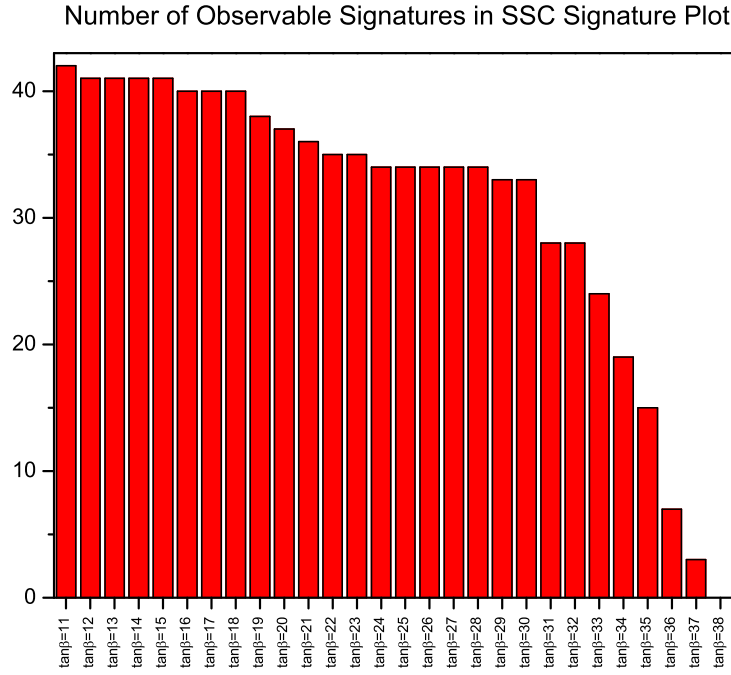


FIG. 8: Number of observable signatures for each spectrum represented in Fig. 7.

TABLE VIII: Superpartner spectra (in GeV) simulated in event generator in Fig. 9 for  $\tan\beta = 34$ .

$m_{1/2}$	$m_0$	$A_0$	$\tan\beta$	$Sgn\mu$	$\Omega_{\chi^0} h^2$	$LSP$
559	322.7	-559	34	+	0.3996	<i>Bino</i>
572	330.2	-572	34	+	0.4508	<i>Bino</i>
585	337.7	-585	34	+	0.5029	<i>Bino</i>
597	344.7	-597	34	+	0.5511	<i>Bino</i>
610	352.2	-610	34	+	0.6013	<i>Bino</i>
621	358.5	-621	34	+	0.6495	<i>Bino</i>
634	366.0	-634	34	+	0.6999	<i>Bino</i>
646	373.0	-646	34	+	0.7528	<i>Bino</i>
658	379.9	-658	34	+	0.8030	<i>Bino</i>
670	386.8	-670	34	+	0.8503	<i>Bino</i>
682	393.8	-682	34	+	0.9027	<i>Bino</i>
694	400.7	-694	34	+	0.9511	<i>Bino</i>

*D6*-brane mass patterns versus the one-parameter model for future work.

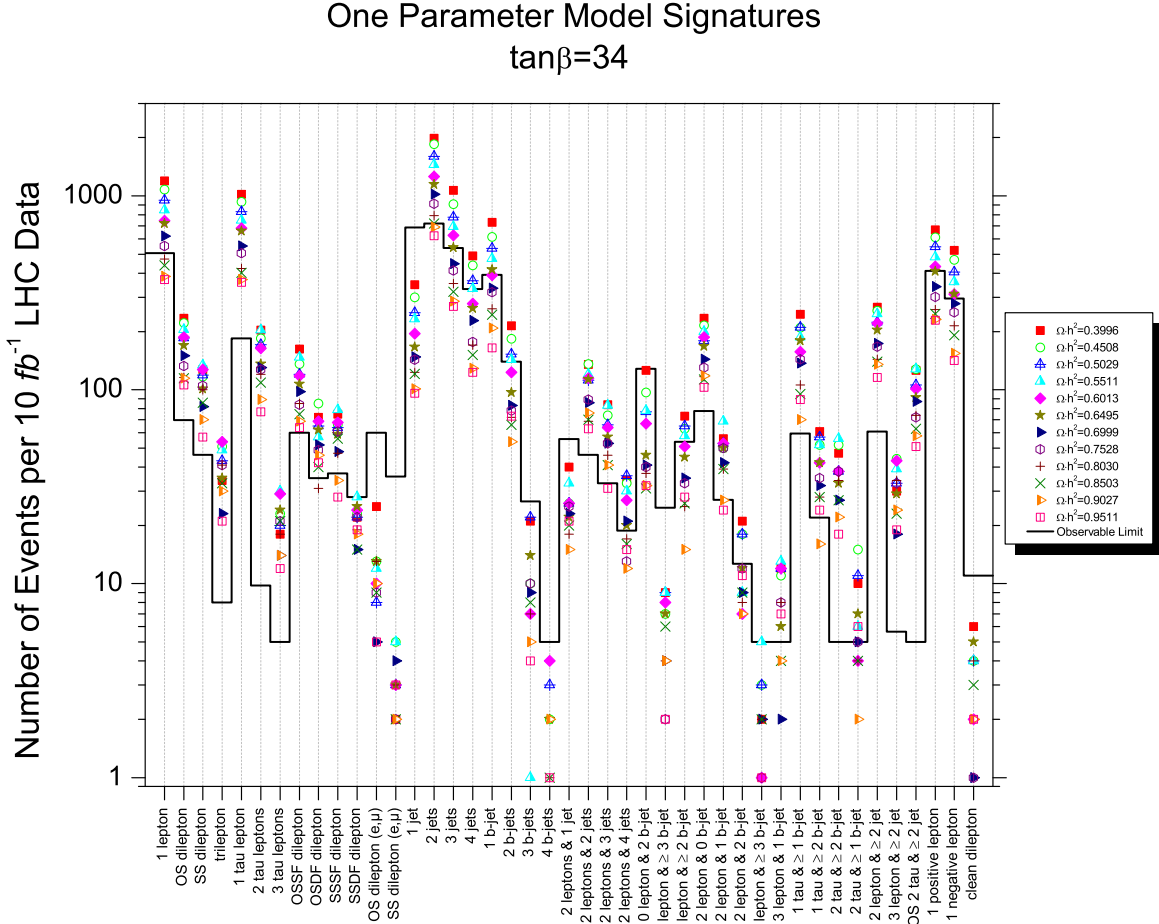


FIG. 9: Signatures of superpartner spectra for  $\tan\beta = 34$  in SSC. Spectra in this plot are listed in Table VIII. The solid bold line represents the observable limit computed in accordance with the requirements in Section III due to the Standard Model background. The markers represent the number of events per 10  $fb^{-1}$  LHC data. An additional cut of  $P_T^{miss} > 275$  GeV was applied in this plot. The number of observable signatures for each spectrum in this plot are shown in Fig. 10.

## VI. CONCLUSION

We have explored the phenomenology of the one-parameter model. Our impetus for carrying out an in-depth study of this model stems from the commonality of the universal soft supersymmetry breaking ansatz across multiple type string compactifications. These include weak coupled and heterotic M-theory vacua, and as well as Type IIB flux vacua, in particular the so-called large-volume compactification models. By performing a comprehensive scan of the entire parameter space and filtering the results according to experimental constraints, the allowed parameter space was obtained. In the strict moduli dominant case, we found that there are no parameter space

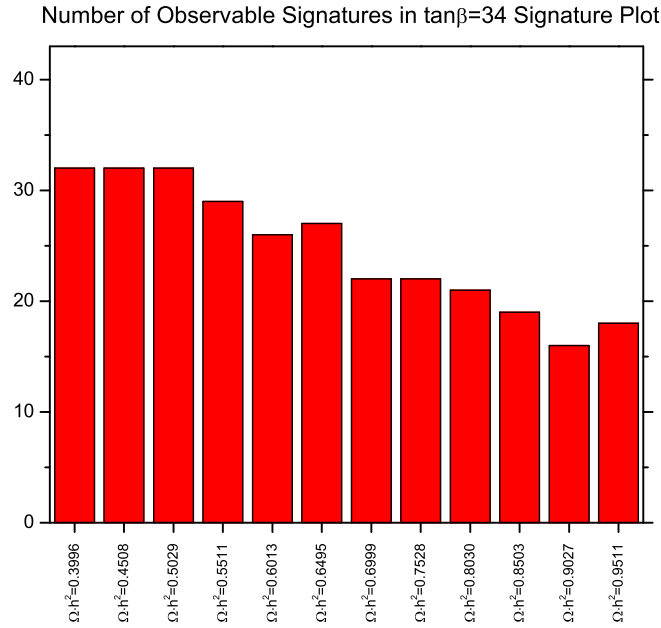


FIG. 10: Number of observable signatures for each spectrum represented in Fig. 9.

TABLE IX: Branching ratios for selected squark decays. These are the ranges of the branching ratios using representative points of the allowed parameter space. If no range is given, then the branching ratio varies by less than 1%. The Squark column represents the specific squark(s) for which that branching ratio is applicable.

Decay Process	Branching Ratio	Squark	Decay Process	Branching Ratio	Squark
$\tilde{q}_L \rightarrow q\tilde{\chi}_1^+$	64% – 65%	$\tilde{q}_L = (\tilde{u}_L, \tilde{d}_L, \tilde{c}_L, \tilde{s}_L)$	$\tilde{q}_R \rightarrow q\tilde{\chi}_1^0$	99%	$\tilde{q}_R = (\tilde{u}_R, \tilde{d}_R, \tilde{c}_R, \tilde{s}_R)$
$\tilde{q}_L \rightarrow q\tilde{\chi}_2^0$	32% – 33%	$\tilde{q}_L = (\tilde{u}_L, \tilde{d}_L, \tilde{c}_L, \tilde{s}_L)$	$\tilde{q}_R \rightarrow t\tilde{\chi}_1^-$	9% – 14%	$\tilde{q}_R = \tilde{b}_2$
$\tilde{q}_L \rightarrow t\tilde{\chi}_1^-$	39% – 42%	$\tilde{q}_L = \tilde{b}_1$	$\tilde{q}_R \rightarrow t\tilde{\chi}_2^-$	20% – 32%	$\tilde{q}_R = \tilde{b}_2$
$\tilde{q}_L \rightarrow t\tilde{\chi}_2^-$	5% – 12%	$\tilde{q}_L = \tilde{b}_1$	$\tilde{q}_R \rightarrow b\tilde{\chi}_4^0$	6% – 10%	$\tilde{q}_R = \tilde{b}_2$
$\tilde{q}_L \rightarrow b\tilde{\chi}_2^0$	22% – 25%	$\tilde{q}_L = \tilde{b}_1$	$\tilde{q}_R \rightarrow \tilde{t}_1 W^-$	22% – 24%	$\tilde{q}_R = \tilde{b}_2$
$\tilde{q}_L \rightarrow \tilde{t}_1 W^-$	16% – 26%	$\tilde{q}_L = \tilde{b}_1$	$\tilde{q}_R \rightarrow b\tilde{\chi}_1^+$	31%	$\tilde{q}_R = \tilde{t}_2$
$\tilde{q}_L \rightarrow b\tilde{\chi}_1^+$	28% – 48%	$\tilde{q}_L = \tilde{t}_1$	$\tilde{q}_R \rightarrow b\tilde{\chi}_2^+$	8% – 12%	$\tilde{q}_R = \tilde{t}_2$
$\tilde{q}_L \rightarrow b\tilde{\chi}_2^+$	1% – 13%	$\tilde{q}_L = \tilde{t}_1$	$\tilde{q}_R \rightarrow t\tilde{\chi}_2^0$	14%	$\tilde{q}_R = \tilde{t}_2$
$\tilde{q}_L \rightarrow t\tilde{\chi}_1^0$	36% – 47%	$\tilde{q}_L = \tilde{t}_1$	$\tilde{q}_R \rightarrow t\tilde{\chi}_4^0$	12% – 13%	$\tilde{q}_R = \tilde{t}_2$
$\tilde{q}_L \rightarrow t\tilde{\chi}_2^0$	12% – 15%	$\tilde{q}_L = \tilde{t}_1$	$\tilde{q}_R \rightarrow \tilde{t}_1 Z^0$	15% – 20%	$\tilde{q}_R = \tilde{t}_2$

which can satisfy all of the constraints, whereas there is a small parameter space allowed for the dilaton scenario. We identified the dominant squark and gluino interactions and presented cascade decay modes that produce lepton signatures. The dominant component of the lepton signatures were tau.

TABLE X: Branching ratios for selected neutralino, chargino, gluino, stop, top, stau, and  $W^+$  decays. These are the ranges of the branching ratios using the representative points of the allowed parameter space. If no range is given, then the branching ratio varies by less than 1%.

Decay Process	Branching Ratio	Decay Process	Branching Ratio
$\tilde{\chi}_1^\pm \rightarrow \tilde{\tau}_1^\pm \nu_\tau$	41% – 96%	$\tilde{g} \rightarrow \tilde{b}_1 \bar{b}$	9% – 10%
$\tilde{\chi}_2^0 \rightarrow \tilde{\tau}_1^- \tau^+$	23% – 48%	$\tilde{g} \rightarrow \tilde{\bar{b}}_1 b$	9% – 10%
$\tilde{\chi}_2^0 \rightarrow \tilde{\tau}_1^+ \tau^-$	23% – 48%	$\tilde{g} \rightarrow \tilde{b}_2 \bar{b}$	6% – 7%
$\tilde{\chi}_2^\pm \rightarrow \tilde{\chi}_1^\pm Z_0$	22% – 27%	$\tilde{g} \rightarrow \tilde{\bar{b}}_2 b$	6% – 7%
$\tilde{\chi}_2^\pm \rightarrow \tilde{\chi}_1^\pm h_0$	22% – 25%	$\tilde{g} \rightarrow \tilde{t}_1 \bar{t}$	14% – 17%
$\tilde{\chi}_2^\pm \rightarrow \tilde{\chi}_2^0 W^\pm$	23% – 31%	$\tilde{g} \rightarrow \tilde{\bar{t}}_1 t$	14% – 17%
$\tilde{\chi}_2^\pm \rightarrow \tilde{\tau}_1^\pm \nu_\tau$	1% – 13%	$\tilde{g} \rightarrow \tilde{t}_2 \bar{t}$	0% – 7%
$\tilde{\chi}_4^0 \rightarrow \tilde{\chi}_1^\pm W^\mp$	21% – 27%	$\tilde{g} \rightarrow \tilde{\bar{t}}_2 t$	0% – 7%
$\tilde{\chi}_4^0 \rightarrow \tilde{\chi}_2^0 h_0$	21% – 24%	$W^+ \rightarrow \bar{d} u$	32%
$\tilde{\chi}_4^0 \rightarrow \tilde{\chi}_1^0 h_0$	6% – 8%	$W^+ \rightarrow \bar{s} c$	32%
$\tilde{\chi}_4^0 \rightarrow \tilde{\tau}_1^\mp \tau^\pm$	1% – 7%	$W^+ \rightarrow e^+ \nu_e$	11%
$t \rightarrow b W^+$	99%	$W^+ \rightarrow \mu^+ \nu_\mu$	11%
$\tilde{\tau}_1^\pm \rightarrow \tilde{\chi}_1^0 \tau^\pm$	100%	$W^+ \rightarrow \tau^+ \nu_\tau$	11%

TABLE XI: Mass patterns of spectra allowed by all constraints for one-parameter model and intersecting  $D6$ -brane model.

Model	Pattern No.	Pattern Type	Mass Pattern
one-parameter	<i>OPMP1</i>	Stau	$\tilde{\chi}_1^0 < \tilde{\tau} < \tilde{e}_R < \tilde{\chi}_1^\pm$
one-parameter	<i>OPMP2</i>	Stau	$\tilde{\chi}_1^0 < \tilde{\tau} < \tilde{e}_R < \tilde{\nu}_\tau$
intersecting $D6$ -brane	<i>ID6BraneP1</i>	Chargino	$\tilde{\chi}_1^0 < \tilde{\chi}_1^\pm < \tilde{\chi}_2^0 < \tilde{\tau}$
intersecting $D6$ -brane	<i>ID6BraneP2</i>	Chargino	$\tilde{\chi}_1^0 < \tilde{\chi}_1^\pm < \tilde{\tau} < \tilde{\chi}_2^0$
intersecting $D6$ -brane	<i>ID6BraneP3</i>	Stau	$\tilde{\chi}_1^0 < \tilde{\tau} < \tilde{\chi}_1^\pm < \tilde{\chi}_2^0$
intersecting $D6$ -brane	<i>ID6BraneP4</i>	Stau	$\tilde{\chi}_1^0 < \tilde{\tau} < \tilde{e}_R < \tilde{\chi}_1^\pm$

We compared the collider signatures of the one-parameter model to those of an intersecting  $D6$ -brane model, which is in some sense equivalent to comparing to wide classes of string vacua to Type IIA compactifications. We found that it may be possible to discriminate between these two types of models. We plan to investigate this possibility more in our future research.

As more realistic string models are developed in the ensuing years, it becomes imperative to distinguish and segregate the pretenders from the contenders, and using phenomenology to simulate the LHC signatures can certainly facilitate the process of determining which vacua of string and M-theory are truly realistic.

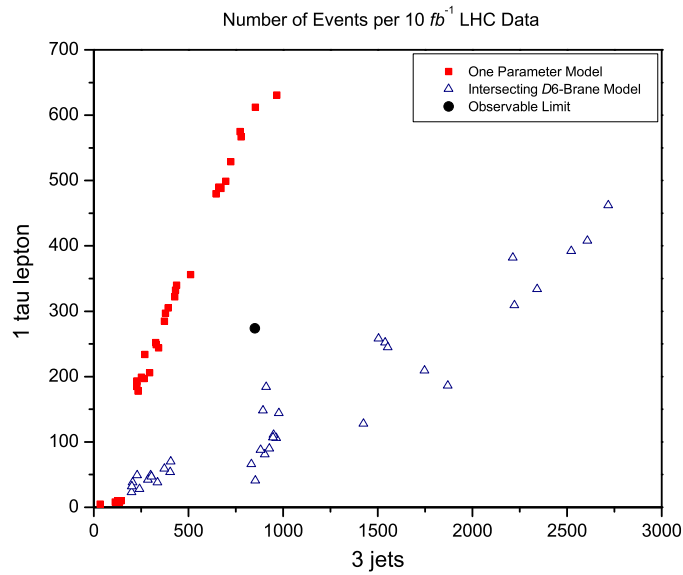


FIG. 11: The number of 1 tau lepton vs. 3 jet events per  $10 \text{ fb}^{-1}$  of integrated luminosity at LHC, for both the intersecting  $D6$ -brane model and the one-parameter model. The round marker indicates the observable limit computed in accordance with the requirements in Section III due to the Standard Model background.

## VII. ACKNOWLEDGMENTS

J.M. would like to thank David Toback for useful discussions regarding particle detector simulations. This research was supported in part by the Mitchell-Heep Chair in High Energy Physics (CMC), by the Cambridge-Mitchell Collaboration in Theoretical Cosmology, and by the DOE grant DE-FG03-95-Er-40917.



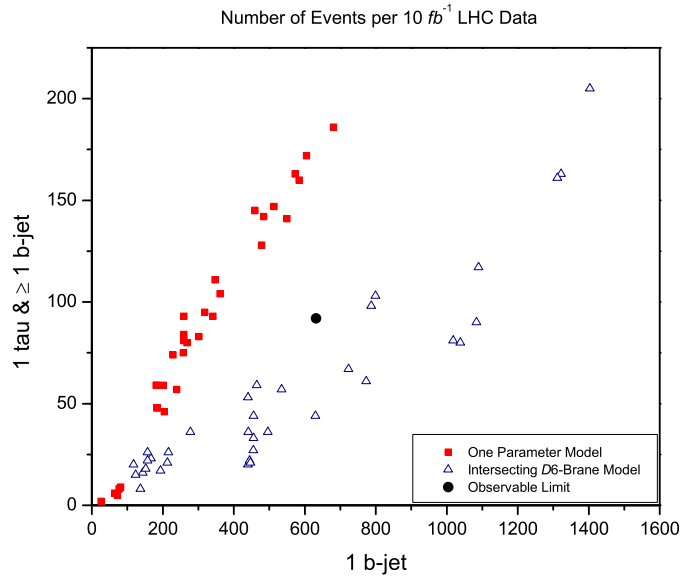


FIG. 12: The number of 1 tau and  $\geq 1$  b-jet vs.  $1 \text{ b-jet}$  events per  $10 \text{ fb}^{-1}$  of integrated luminosity at LHC, for both the intersecting  $D6$ -brane model and the one-parameter model. The round marker indicates the observable limit computed in accordance with the requirements in Section III due to the Standard Model background.

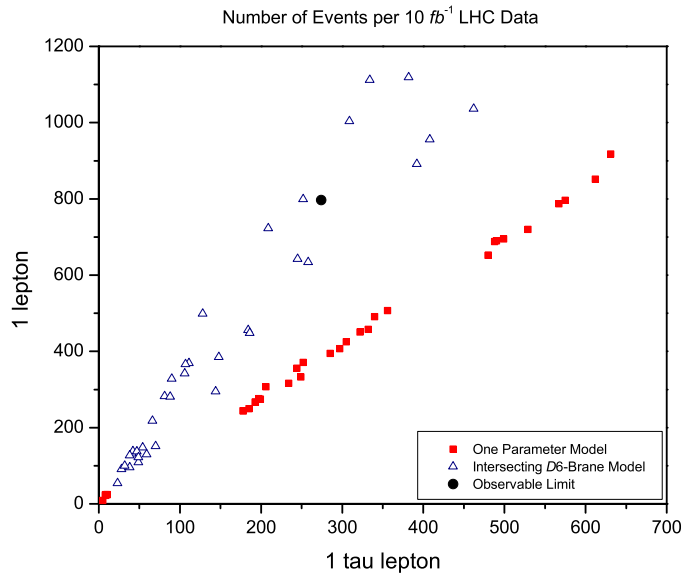


FIG. 13: The number of 1 lepton vs.  $1 \text{ tau lepton}$  events per  $10 \text{ fb}^{-1}$  of integrated luminosity at LHC, for both the intersecting  $D6$ -brane model and the one-parameter model. The round marker indicates the observable limit computed in accordance with the requirements in Section III due to the Standard Model background.

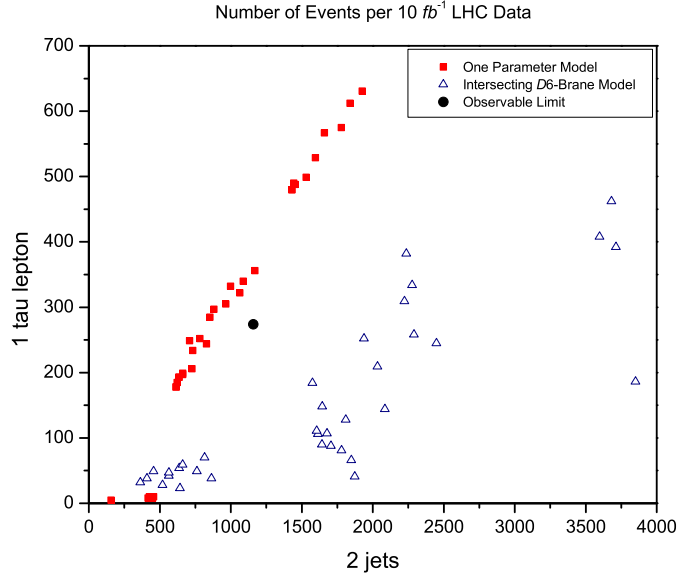


FIG. 14: The number of 1 tau lepton vs. 2 jet events per  $10 \text{ fb}^{-1}$  of integrated luminosity at LHC, for both the intersecting  $D6$ -brane model and the one-parameter model. The round marker indicates the observable limit computed in accordance with the requirements in Section III due to the Standard Model background.

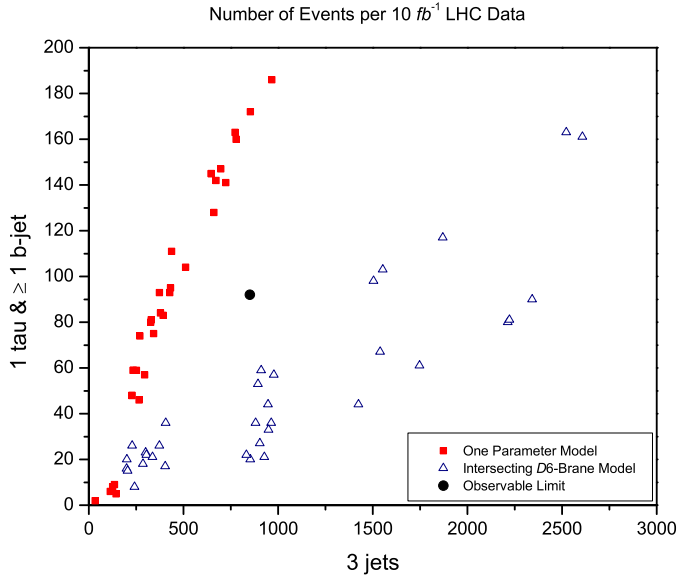


FIG. 15: The number of 1 tau and  $\geq 1$  b-jet vs. 3 jet events per  $10 \text{ fb}^{-1}$  of integrated luminosity at LHC, for both the intersecting  $D6$ -brane model and the one-parameter model. The round marker indicates the observable limit computed in accordance with the requirements in Section III due to the Standard Model background.

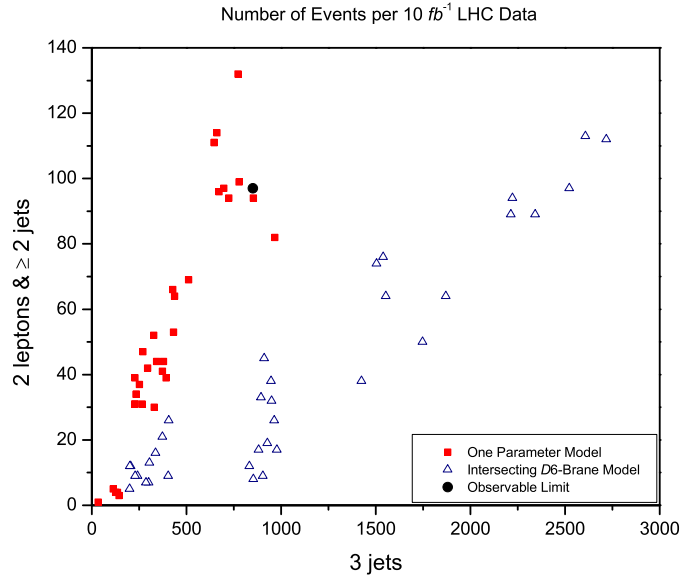


FIG. 16: The number of 2 leptons and  $\geq 2$  jets vs. 3 jet events per  $10 \text{ fb}^{-1}$  of integrated luminosity at LHC, for both the intersecting  $D6$ -brane model and the one-parameter model. The round marker indicates the observable limit computed in accordance with the requirements in Section III due to the Standard Model background.

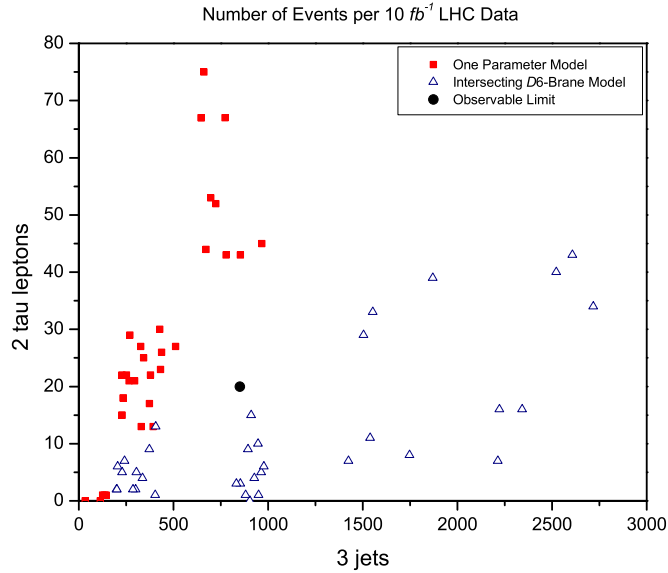


FIG. 17: The number of 2 tau leptons vs. 3 jet events per  $10 \text{ fb}^{-1}$  of integrated luminosity at LHC, for both the intersecting  $D6$ -brane model and the one-parameter model. The round marker indicates the observable limit computed in accordance with the requirements in Section III due to the Standard Model background.

- 
- [1] J. R. Ellis, D. V. Nanopoulos and K. Tamvakis, Phys. Lett. B **121**, 123 (1983).
  - [2] J. R. Ellis, J. S. Hagelin, D. V. Nanopoulos and K. Tamvakis, Phys. Lett. B **125**, 275 (1983).
  - [3] L. Alvarez-Gaume, J. Polchinski and M. B. Wise, Nucl. Phys. B **221**, 495 (1983).
  - [4] E. Cremmer, S. Ferrara, C. Kounnas, and D. V. Nanopoulos, Phys. Lett. B **133**, (1983) 61; J. Ellis, A. Lahanas, D. V. Nanopoulos, and K. Tamvakis, Phys. Lett. B **134**, (1984) 429; J. Ellis, C. Kounnas, and D. V. Nanopoulos, Nucl. Phys. B **241**, (1984) 406 and B **247** (1984) 373; For a review see A. Lahanas and D. V. Nanopoulos, Phys. Rep. **145**, (1987) 1
  - [5] J. L. Lopez and D. V. Nanopoulos, Int. J. Mod. Phys. A **11**, (1996) 3439-3478. arXiv:hep-ph/9412332v2
  - [6] V. Kaplunovsky and J. Louis, Phys. Lett. B **306**, (1993) 269. arXiv:hep-th/9303040v1
  - [7] A. Brignole, L. Ibáñez, and C. Munõz, Nucl. Phys. B **422**, (1994) 125. arXiv:hep-ph/9707209
  - [8] V. Balasubramanian, P. Berglund, J. P. Conlon and F. Quevedo, JHEP **0503**, (2005) 007. arXiv:hep-th/0502058
  - [9] J. P. Conlon, F. Quevedo, and K. Suruliz, JHEP **0508**, (2005) 007. arXiv:hep-th/0505076
  - [10] J. R. Ellis and D. V. Nanopoulos, Phys. Lett. B **110**, 44 (1982).
  - [11] I. Antoniadis, J. R. Ellis, J. S. Hagelin and D. V. Nanopoulos, Phys. Lett. B **194** (1987) 231; Phys. Lett. B **205** (1988) 459; Phys. Lett. B **208** (1988) 209 [Addendum-ibid. B **213** (1988) 562]; Phys. Lett. B **231** (1989) 65.
  - [12] Tianjun Li, Phys. Rev. **D59**, (1999) 107902. arXiv:hep-ph/9804243v1
  - [13] J. P. Conlon, S. S. Abdussalam, F. Quevedo, and K. Suruliz, JHEP **0701**, (2007) 032. arXiv:hep-th/0610129v2
  - [14] L. Aparicio, D. G. Cerdeno and L. E. Ibanez, JHEP **0807**, 099 (2008) [arXiv:0805.2943 [hep-ph]].
  - [15] C. Beasley, J. J. Heckman and C. Vafa, arXiv:0806.0102 [hep-th].
  - [16] C. M. Chen, T. Li, V. E. Mayes and D. V. Nanopoulos, Phys. Lett. B **665**, 267 (2008) [arXiv:hep-th/0703280]; Phys. Rev. D **77**, 125023 (2008) [arXiv:0711.0396 [hep-ph]].
  - [17] J. L. Lopez, D. V. Nanopoulos and A. Zichichi, Phys. Lett. B **319** (1993) 451 [arXiv:hep-ph/9306226].
  - [18] J. L. Lopez, D. V. Nanopoulos and A. Zichichi, Int. J. Mod. Phys. A **10**, 4241 (1995) [arXiv:hep-ph/9408345].
  - [19] J. L. Lopez, D. V. Nanopoulos and A. Zichichi, Phys. Rev. D **52**, 4178 (1995) [arXiv:hep-ph/9502414]; For a review, see *Searching for the Superworld: A Volume in Honor of Antonino Zichichi on the Occasion of the Sixth Centenary Celebrations of the University of Turin, Italy*, Antonino Zichichi, Sergio Ferrara, Rudolf M. Mössbauer, World Scientific (2007), ISBN 9812700188, 9789812700186
  - [20] G. Blanger, F. Boudjema, A. Pukhov, A. Semenov, Comput. Phys. Commun. **176**, (2007) 367-382.

- arXiv:hep-ph/0607059; G. Blanger, F. Boudjema, A. Pukhov, A. Semenov, Comput. Phys. Commun. **174**, (2006) 577. arXiv:hep-ph/0405253; G. Blanger, F. Boudjema, A. Pukhov, A. Semenov, Comput. Phys. Commun. **149**, (2002) 103. arXiv:hep-ph/0112278
- [21] A. Djouadi, J. Kneur, and G. Moultaka, Comput. Phys. Commun. **176**, (2007) 426-455. arXiv:hep-ph/0211331v2
- [22] G. Hinshaw *et al*, arXiv:hep-th/0803.0732v1[astro-ph]
- [23] D. N. Spergel *et al* [WMAP Collaboration], Astrophys. J. Suppl. **170**, 377 (2007) arXiv:astro-ph/0302209; astro-ph/0603449v2.
- [24] I. Antoniadis, C. Bachas, J. R. Ellis, and D. V. Nanopoulos, Phys. Lett. B **211** (1988) 393; Nucl. Phys. B **328** (1989) 117; Phys. Lett. B **257** (1991) 278; J. R. Ellis, N.E. Mavromatos, and D. V. Nanopoulos, Lectures given at International Workshop on Recent Advances in the Superworld, Woodlands, TX, 13-16 Apr 1993, Published in Woodlands Superworld 1993:3-26 (QCD161:I966:1993) e-Print: hep-th/9311148; J. R. Ellis, N. E. Mavromatos, and D. V. Nanopoulos, Mod. Phys. Lett. A **10** (1995) 1685; Phys. Lett. B **619** (2005) 17; D. V. Nanopoulos and D. Xie, Phys. Rev. D **78**, 044038 (2008) [arXiv:0710.2312 [hep-th]].
- [25] A. B. Lahanas, N. E. Mavromatos, and D. V. Nanopoulos, PMC Phys. A **1** (2007) 2; Phys. Lett. B **649** (2007) 83;
- [26] B. Dutta, A. Gurrola, T. Kamon, A. Krislock, A. B. Lahanas, N. E. Mavromatos and D. V. Nanopoulos, arXiv:0808.1372 [hep-ph].
- [27] E. Barberio, *et al* (Heavy Flavor Averaging Group), arXiv:hep-ex/0704.3575v1
- [28] M. Misiak *et al*, Phys. Rev. Lett. **98**, 022002 (2007). arXiv:hep-ph/0609232v2
- [29] G. W. Bennett *et al* (Muon g-2 Collaboration), Phys. Rev. Lett. **92**, 161802 (2004). arXiv:hep-ex/0401008
- [30] The CDF Collaboration, Phys. Rev. Lett. **95**, 221805 (2005) [Erratum-ibid. **95** (2005) 249905]. arXiv:hep-ex/0508036v3
- [31] R. Barate *et al* (LEP Working Group for Higgs boson searches) Phys. Lett. B **565**, 61 (2003), arXiv:hep-ex/0306033; W. M. Yao *et al* (Particle Data Group), J. Phys. G **33**, 1 (2006).
- [32] B. Dutta, Y. Mimura and D. V. Nanopoulos, Phys. Lett. B **656**, 199 (2007) [arXiv:0705.4317 [hep-ph]].
- [33] T. Sjostrand, S. Mrenna, and P. Skands, JHEP **0605**, (2006) 026. arXiv:hep-ph/0603175v2
- [34] <http://www.physics.ucdavis.edu/~conway/research/software/pgs/pgs4-general.htm>
- [35] P. Skands *et al*, JHEP **0407**, (2004) 036. arXiv:hep-ph/0311123v3
- [36] [http://v1.jthaler.net/olympicswiki/doku.php?id=lhc\\_olympics:trigger\\_table#what\\_are\\_triggers](http://v1.jthaler.net/olympicswiki/doku.php?id=lhc_olympics:trigger_table#what_are_triggers)
- [37] [http://v1.jthaler.net/olympicswiki/doku.php?id=lhc\\_olympics:chroot](http://v1.jthaler.net/olympicswiki/doku.php?id=lhc_olympics:chroot)
- [38] <http://wwwphy.princeton.edu/~verlinde/research/lhco/BOXC/>
- [39] G. Kane, P. Kumar, and J. Shao, arXiv:hep-ph/0709.4259v1

- [40] D. Feldman, Z. Liu, and P. Nath, Phys. Rev. Lett. **99**, 251802 (2007). arXiv:hep-ph/0707.1873v3